

**A Comparison Between the
Williamson-Hall and
Warren-Averbach Methods for XRD
Analysis of TiAlN Samples**

Mini Thesis

Caglayan ARAS

Supervisors:

Pavel Ondračka, Ph.D.

Jochen M. Schneider, Prof.

RWTH Aachen, Materials Chemistry

01/04/2020

Contents

List of Figures	ii
List of Tables	iii
1 Introduction	2
1.1 Goal	2
1.2 Motivation	2
1.3 Strategy	2
2 Theoretical Background of Diffraction by Imperfect Crystals	3
2.1 Bragg's Law	3
2.2 Atomic Form and Structure Factors	5
2.3 Profile Fitting and Instrumental Broadening	9
2.4 Particle Size Broadening and Scherrer Formula	11
2.5 Williamson-Hall Model	14
2.6 Warren-Averbach Model	17
2.6.1 Estimation of Crystallite Size Distribution	19
3 Results and Discussion	22
3.1 Experimental Details	22
3.2 Crystallite Size Comparison	23
3.3 Microstrain Comparison	26
3.4 Conclusion & Future Work	29
A Appendix	31
B Appendix	33
References	35

List of Figures

1	Phase difference in an electron cloud.	3
2	θ - θ condition. Plane normal and $\Delta\mathbf{k}$ are in the same direction.	4
3	A layer of all-electron charge density in TiAlN supercell.	6
4	Phase shift at different incidence angles	6
5	Atomic form factors of Ti, Al and N	7
6	Calculated vs measured diffraction pattern	8
7	Instrumental broadening. GADDS versus D5000	10
8	Wave-vectors in the derivation of Scherrer formula.	12
9	Williamson-Hall plot	15
10	First and second type of imperfections.	16
11	Summary of Warren-Averbach analysis.	18
12	Log-normal distribution of crystallite size.	21
13	Hook effect observed in D5000 measurements.	22
14	Measured diffractograms at different annealing samples.	23
15	Williamson - Hall plot of as deposited TiAlN sample.	24
16	Size coefficients of as deposited sample.	25
17	Microstrain at different annealing temperatures.	26
17	RMS of strain at different annealing temperatures. (cont.)	27
18	Physical meaning of calculated strains.	27
19	2D explanation of increased strain gap at higher annealing temperatures.	28

List of Tables

1	Diffraction line profile parameters	5
2	Calculated average crystallite sizes	25

Abstract

TiAlN coatings are widely used in industry for cutting tools due to their excellent oxidation resistance and hardness at elevated temperatures. X-ray diffraction (XRD) is a routine tool in analysis of crystal structure and lattice parameters, but can also provide information about other microstructure parameters, such as microstrain and crystallite size, which play a significant role in coating properties. In this work, different line profile analysis (LPA) methods such as Scherrer equation, Williamson-Hall model and Warren-Averbach analysis are used to obtain microstructure information from X-ray diffraction patterns of TiAlN powder samples, previously synthesized by high power pulsed magnetron sputtering and annealed at different temperatures. Measurements were done with Siemens D5000 diffractometer and Bruker AXS D8 General Area Detection Diffraction System (GADDS) and the instrumental effects on broadening of the line profiles were compared and deconvoluted from the measured profiles. A thorough evaluation of the different methods was done and showed that while Scherrer equation and Williamson-Hall models are easy to apply, they do not yield a comprehensive set of information about the microstructure. Warren-Averbach analysis, which is a Fourier analysis of the line profiles provides a more extensive set of information including crystallite size distribution and microstrain at different lengths under some assumptions. However, it is very sensitive to the measured background and was only applicable to the GADDS data, not possible for the D5000 measurements.

The Warren-Averbach analysis revealed that average number of coherent planes in the sample set is larger in $\{111\}$ compared to $\{200\}$. Moreover, more equiaxed crystallites are formed at high annealing temperatures. It has also been observed that microstrain decreases in sample annealed at 710 °C. As the annealing temperature increases to 1060 °C, microstrain in $[100]$ significantly increases while there is no significant change in $[111]$, indicating that c-AlN clusters on $\{200\}$ as spinodal decomposition starts.

1 Introduction

The infinite variety in the properties of the solid materials we find in the world is really the expression of the infinite variety of the ways in which the atoms and molecules can be tied together, and of the strength of those ties.

William Henry Bragg, Concerning The Nature of Things - 1925

1.1 Goal

The goal of this study is to give an overview of the fundamentals of X-Ray diffraction and compare different size & strain analysis methods such as Scherrer law, Williamson-Hall model and Warren-Averbach analysis on TiAlN powder samples annealed at different temperatures.

1.2 Motivation

In June 2011, Materials Genome Initiative [1] was launched to help researchers to discover and develop new materials faster. Today, it makes literally hundreds of thousands of density functional theory (DFT) calculations accessible and allows us to exploit machine learning algorithms in material science. Information of crystal structure plays an essential role in developed models and has to be mathematically well represented. X-Ray diffraction not only helps us to characterize the structure of the material, but also sheds light on the mathematical nature of periodicity of the crystals. Additionally, material properties are highly influenced by crystallite size and imperfections in the crystal which is another reason why they should be investigated.

1.3 Strategy

Previously synthesized $Ti_{0.5}Al_{0.5}N$ powder samples are measured by Siemens D5000 and Bruker D8 GADDS diffractometers. All models are implemented from scratch and no commercial program is used. Relevant code can be found on author's GitHub page¹.

¹<https://github.com/caglayanoaras/XRD>

2 Theoretical Background of Diffraction by Imperfect Crystals

2.1 Bragg's Law

An X-ray beam is an electromagnetic wave composed of electric and magnetic field perpendicular to each other and varying sinusoidally in the direction perpendicular to the propagation. Scattering physics of the X-ray can be explained in terms of classical electrodynamics. An electric field exerts force on a charged particle, oscillating electric field of X-ray puts electrons into oscillatory motion and accelerated electrons emit electromagnetic waves. Compared to the electron, nuclei of the atoms have larger mass and their acceleration is negligible. The scattered beam has the same wavelength and the frequency as the incident beam and is said to be coherent with it [2]. Another way in which electrons can scatter X-rays is called Compton or incoherent scattering and it is not discussed in this study.

Figure 1 shows an arbitrary shaped electron density with point O as the defined origin. \mathbf{k} and \mathbf{k}' are incident and scattered wave vectors respectively. Since scattering is elastic, wavenumbers of wave vectors are the same and equal to $\frac{2\pi}{\lambda}$. Dashed red lines are the parallel directions to the wave vectors and \mathbf{u} and \mathbf{u}' are unit vectors having the same direction with wave vectors. Phase factor of any arbitrary infinitesimal volume dV at any arbitrary point \mathbf{R} can be

written in exponential form $\exp(-i\frac{2\pi}{\lambda}\Delta\mathbf{u} \cdot \mathbf{R})$ where $\Delta\mathbf{u} = \mathbf{u}' - \mathbf{u}$. Total amplitude of

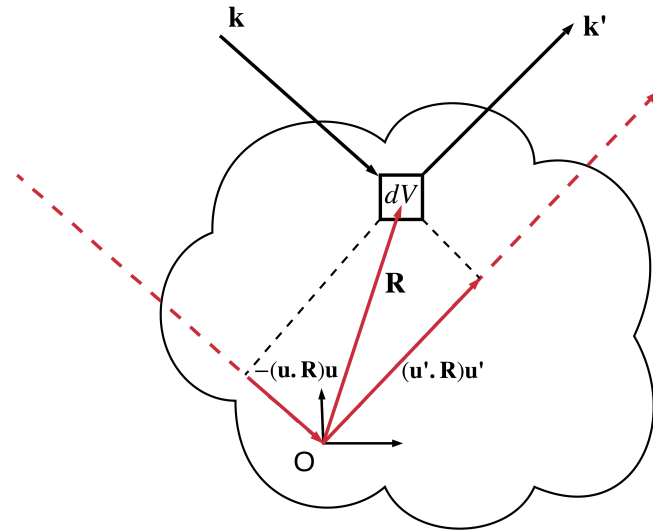


Figure 1: Phase difference in an electron cloud.

scattering requires summation over all volume and can be written as

$$F(\Delta\mathbf{k}) = \int_V \rho(\mathbf{R}) e^{-i\Delta\mathbf{k}\cdot\mathbf{R}} dV, \quad (1)$$

where: $\rho(\mathbf{R})$ = electron density at position \mathbf{R} .

Equation (1) shows that the amplitude of scattering is the Fourier transform of electron density. For crystal structures electron density is periodic in space:

$$\rho(\mathbf{R}) = \rho(\mathbf{R} + \mathbf{r}) \quad (2)$$

or in Fourier series:

$$\rho(\mathbf{R}) = \sum_{\mathbf{G}} \rho_{\mathbf{G}} e^{i\mathbf{G}\cdot\mathbf{R}} \quad (3)$$

where: \mathbf{G} = reciprocal lattice vectors,

$\rho_{\mathbf{G}}$ = corresponding Fourier coefficients.

Substituting electron density in Equation (1) with Equation (3) leads to

$$F(\Delta\mathbf{k}) = \sum_{\mathbf{G}} \rho_{\mathbf{G}} \int_V e^{i(\mathbf{G}-\Delta\mathbf{k})\cdot\mathbf{R}} dV. \quad (4)$$

For large crystal structures, when $\Delta\mathbf{k}$ is equal to a particular reciprocal lattice vector, F will be non zero and will be equal to $V\rho_{\mathbf{G}}$. Otherwise F is zero. If there were a way to measure Fourier coefficients $\rho_{\mathbf{G}}$, then it would be possible to construct the electron density function. $\rho_{\mathbf{G}}$ coefficients are complex numbers and the measured intensity is proportional to the amplitudes of these coefficients ($I \propto F^2 \propto V^2|\rho_{\mathbf{G}}|^2$), so phase information of the coefficients can not be obtained with XRD measurements. This is called the phase problem and it is the central problem in

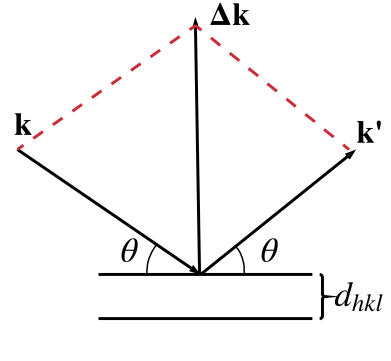


Figure 2: θ - θ condition. Plane normal and $\Delta\mathbf{k}$ are in the same direction.

interpretation of crystal diffraction data [3].

For infinitely large periodic electron densities, Bragg's law can easily be deduced from Equation (4). Writing $\Delta\mathbf{k}$ in terms of scattering and incidence angle θ yields (Figure 2)

$$|\Delta\mathbf{k}| = \frac{4\pi}{\lambda} \sin \theta. \quad (5)$$

Hence, an alternative version of $|\Delta\mathbf{k}| = |\mathbf{G}|$ can be written, which is also known as Bragg's law:

$$\frac{4\pi}{\lambda} \sin \theta = \frac{2\pi}{d_{hkl}}. \quad (6)$$

Bragg's law is useful for determination of lattice parameters, but it does not yield any information about the microstrain, crystallite size and lattice defects. Table 1 summarizes the use of diffraction line profiles [4].

Table 1: Diffraction line profile parameters

Position	Intensity	Shape	Shift	Method	Identification
+				Indexing	Cell parameters
+	+			Phase analysis	Quantity
			+	Peak-shift analysis	Residual stress
+		+		Profile analysis	Size, Microstrain
+	+	+		Structure refinement	Atomic positions

2.2 Atomic Form and Structure Factors

If Equation (1) is written for a single atom, the result is defined as atomic form factor. In other words, the atomic form factor is the Fourier transform of the electron density of an atom. The values of atomic form factors for free atoms and chemically significant ions can be found at International Tables for Crystallography (ICT) [5]. These numbers are the result of quantum mechanical calculations where the electron densities are spherically symmetric.

Equation (7) is used for analytical approximation of calculated form factors.

$$f\left(\frac{\sin \theta}{\lambda}\right) = \sum_{i=1}^4 a_i \exp\left(\frac{-b_i \sin^2 \theta}{\lambda^2}\right) + c \quad (7)$$

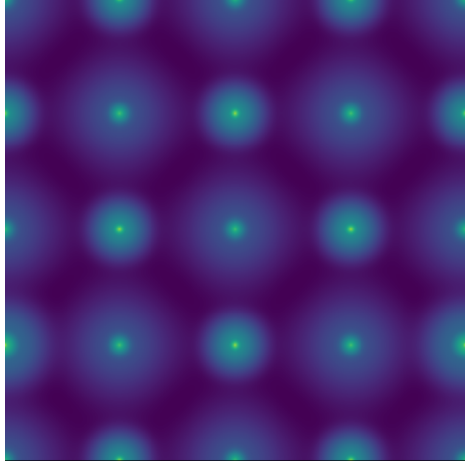
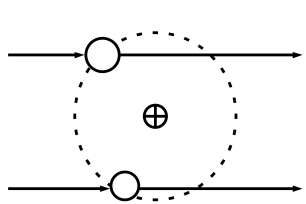


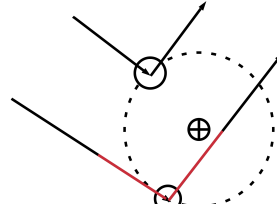
Figure 3: A layer of all-electron charge density in TiAlN supercell.

The free atom assumption naturally raises questions about the reliability of the calculations. However, according to Kittel [6], X-ray intensities are represented well by free atom calculations and do not change too much with small re-distributions of electrons. In order to analyse how perturbation of the electron density by interaction with other atoms affects the scattering, the ground state electron charge density is calculated for a $\text{Ti}_{0.5}\text{Al}_{0.5}\text{N}$ cell with 64 atom using the density functional theory (DFT) [7]. The cell is generated using the special quasi-random structure (SQS) method [8]. The

exchange-correlation effects were included at the level of generalized gradient approximation with the parametrization by Perdew, Burke and Ernzerhof [9]. The plane-wave energy cutoff was set to 500 eV with Monkhorst-Pack k -point grid $6\times 6\times 6$, and the total energy convergence criterion of less than 0.1 meV per atom. The all electron charge density was calculated on a fine $768\times 768\times 768$ grid.



(a) There is no phase shift when θ is zero



(b) Phase shift occurs if θ is non-zero.

Figure 4: Phase shift at different incidence angles

Equation (7) works well for the analytical approximation of the calculated atomic form

factors. Figure 5 shows the *ab initio* form factors of Ti, Al and N atoms along with results generated using ICT tables. When the incident angle is zero, atomic form factor will be equal to the total number of electrons because there is no phase shift (Figure 4a). As $|\Delta\mathbf{k}|$ increases, scattered intensity will decrease since destructive interference occurs due to the phase shift (Figure 4b).

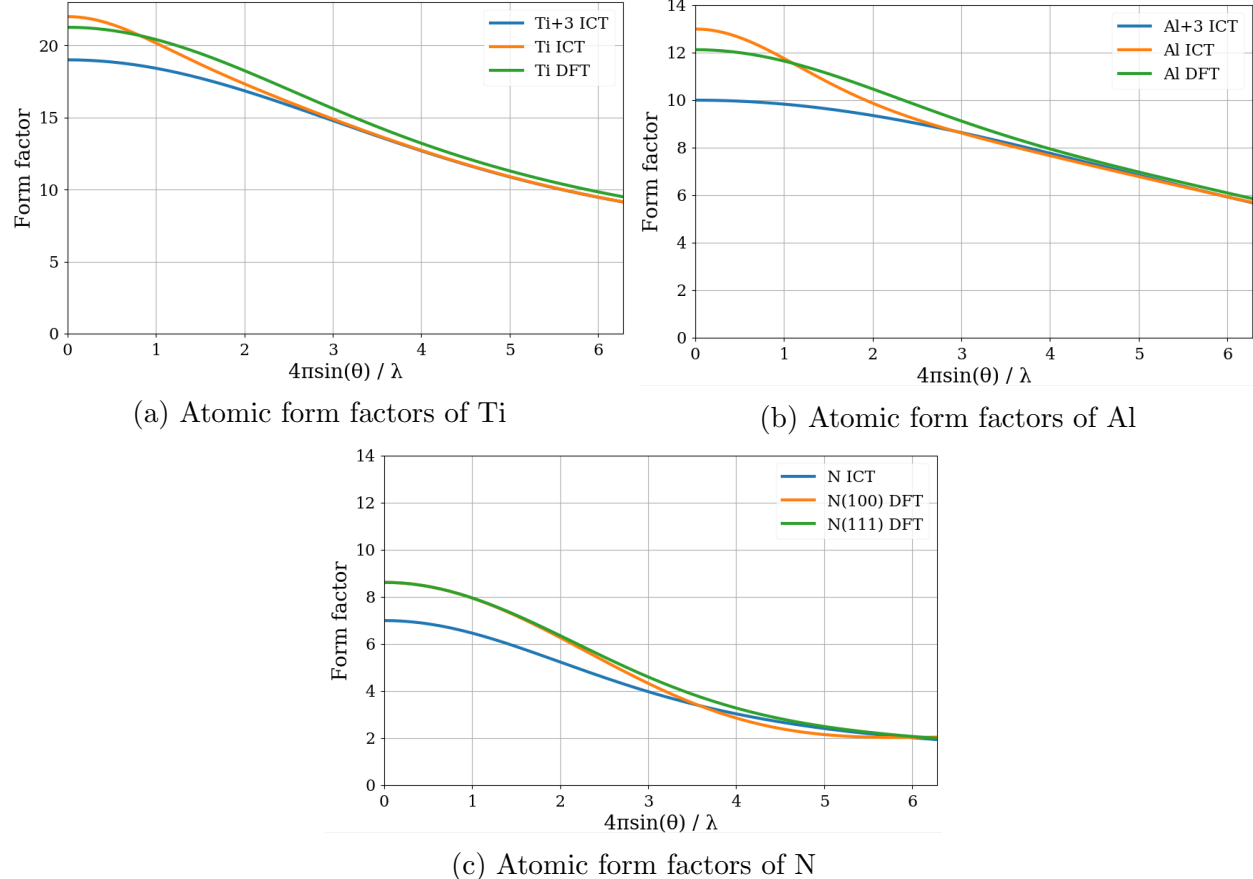


Figure 5: Atomic form factors of Ti, Al and N

The structure factor is defined as the result of Equation (1) integrated over the volume of a unit cell. It can be written in terms of atomic form factors

$$F(\Delta\mathbf{k}) = \sum_{n=1}^N f_n(\Delta\mathbf{k}) e^{-i\Delta\mathbf{k}\cdot\mathbf{r}_n}, \quad (8)$$

where: N = total number of atoms in unit cell,

\mathbf{r}_n = position of the n^{th} atom,

f_n = atomic form factor of the n^{th} atom.

For a set of atoms, the scattered intensity is the structure factor multiplied with its complex conjugate

$$I(\Delta\mathbf{k}) = \sum_{m=1}^N \sum_{n=1}^N f_n(\Delta\mathbf{k}) f_m(\Delta\mathbf{k}) e^{-i\Delta\mathbf{k}\cdot(\mathbf{r}_n - \mathbf{r}_m)}. \quad (9)$$

Unfortunately, there are different definitions for structure factor in literature. In crystal community it is generally defined as above and is equal to the amplitude. Whereas in non-crystal materials community it is generally represented as $S(\Delta\mathbf{k})$ and is equal to the scattering intensity ($|F(\Delta\mathbf{k})|^2$) [10].

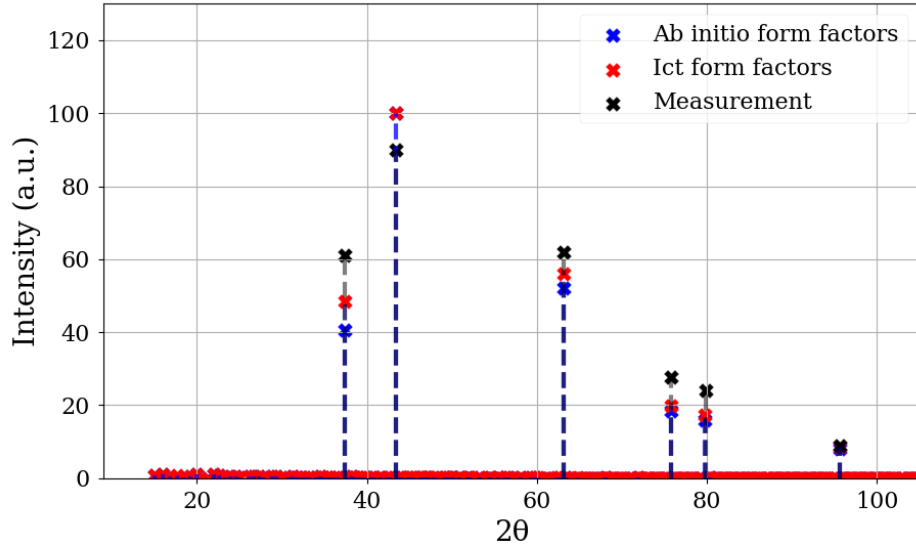


Figure 6: Calculated vs measured diffraction pattern

Figure 6 shows the measured diffraction pattern, *ab initio* diffraction pattern calculated for 64 atom SQS structure, and calculation using ICT free atom form factors for the same SQS structure. Even though the intensities are highly correlated, they do not match perfectly. There are a few possible explanations. Exact chemical composition might be slightly different, incoherent scattering is not taken into account, Debye-Waller factors are taken as zero and finally polarization and absorption factors might be different than the textbook calculations that can lead a propagation in error. Observed peaks are all fundamental peaks and shuffling Ti and Al atoms in the structure does not change the calculated intensities. Thus, short range ordering or the distribution of the metal ions can not be the reason for the deviation of the intensities in Figure 6.

2.3 Profile Fitting and Instrumental Broadening

First step of the size-strain analysis is fitting commonly used model functions to the measured data. Gaussian and Lorentzian functions are the two commonly used mathematical functions [11].

$$I_{\text{Lorentzian}}(\alpha) = \frac{I_0}{1 + 4 \left(\frac{\alpha - 2\theta}{w} \right)^2} \quad (10)$$

$$I_{\text{Gaussian}}(\alpha) = I_0 \exp \left[-4 \ln 2 \left(\frac{\alpha - 2\theta}{w} \right)^2 \right] \quad (11)$$

where: I_0 = maximum intensity,
 w = full width at half maximum,
 α = diffraction angle.

Pseudo-Voigt function is defined as a linear combination of Gaussian and Lorentzian functions. In this study, pseudo-Voigt function is used as a model function. Levenberg-Marquardt algorithm is implemented in order to fit the measured data points [12]. Appendix A shows the fitted versus measured diffractogram of the same sample measured with different instruments. A 6th order polynomial is used for fitting the background.

Line profiles of the diffractogram do not only depend on the sample. They are also affected by instrumental setup such as:

- Emission profile of the tube,
- Widths of the divergence and receiving slit,
- Aperture of Soller slits,
- Filters and monochromators on the beam path,
- All other factors which does not depend on the measured sample[13].

Samples are measured using Siemens D5000 and Bruker GADDS D8 diffractometers. Both of them use copper as radiation source and K α emission line is an important source of instru-

mental broadening. Cu K α_2 component can be eliminated using commercial Diffrac.suite Eva program. In order to be able to determine broadening due to other factors, a standard sample should be measured. The standard sample used for line profile analysis should not exhibit size broadening or strain broadening. Two common example for that type of material is NIST SRT 660 (Lanthanum hexaboride) [14] and NIST 1976b (Corundum) [15]. In this study polycrystalline Al₂O₃ plate is used for detection of instrumental broadening. The measurement of Al₂O₃ yields a full width at half maximum (FWHM) versus 2θ curve. Equation (12) is fitted to this curve.

$$w_{inst}^2 = U \tan^2 \theta + V \tan \theta + W \quad (12)$$

where: w_{inst} = FWHM of instrumental broadening.

This equation is also known as Caglioti equation [16] and was developed for neutron diffraction patterns originally. It is possible to find other fitting functions in the literature [17].

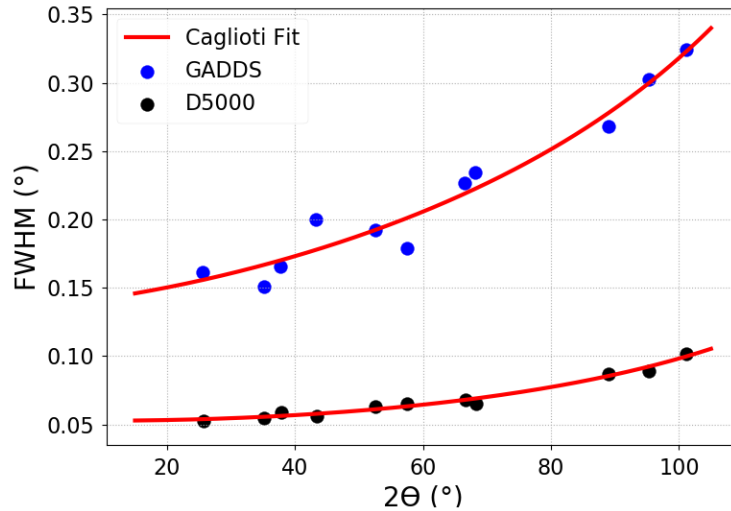


Figure 7: Instrumental broadening. GADDS versus D5000

Figure 7 shows FWHM versus 2θ curve for D5000 and GADDS measurements of the same standard sample. It is observed that profiles measured with GADDS have larger FWHM than D5000 on average. Thus, it is necessary to take into account the instrumental broadening.

If profiles are assumed to be Lorentzian, relationship between the instrumental, sample and profile broadening can be written as

$$w_{\text{profile}} = w_{\text{sample}} + w_{\text{instrument}}. \quad (13)$$

If profiles are assumed to be Gaussian,

$$w_{\text{profile}}^2 = w_{\text{sample}}^2 + w_{\text{instrument}}^2. \quad (14)$$

Real profiles are neither Gaussian nor Lorentzian and direct subtraction of FWHM values might lead to erroneous results. In order to get more reliable results, instrumental broadening has to be deconvoluted from the measured profile. Fourier transform of the measured profile is divided by the Fourier transform of instrumental profile and inverse Fourier transform of calculated function is taken in order to get the broadening due to the sample.

2.4 Particle Size Broadening and Scherrer Formula

In real world measurements, observed Bragg peaks are not Dirac delta functions such as in Figure 6. They are rather broader functions and one reason for that is the sufficiently small crystallite sizes. This relation is known as the Scherrer formula [18] and is used intensively in the literature.

For simplicity let's assume $(00l)$ plane in an orthorhombic cell with N planes. Equation (9) yields

$$I(\Delta\mathbf{k}) = \overline{f(\Delta\mathbf{k})}^2 \sum_{n=1}^N e^{-iqdn} \sum_{m=1}^N e^{iqdm}, \quad (15)$$

where: $\overline{f(\Delta\mathbf{k})}$ = Average form factor of the atoms on the plane,

d = d spacing of the plane $(00l)$,

dn = Position of the n^{th} plane, in the coordinate system,

q = $|\Delta\mathbf{k}|$.

Atomic form factors are taken outside of the summation because it is assumed that atoms

are uniformly distributed and that every plane has the same chemical composition. As a result form factor is the same for each plane. The complex exponential series in equation (15) can also be written as

$$\sum_{n=1}^N e^{-iqdn} = \frac{e^{iqd} - e^{iqd(N+1)}}{1 - e^{iqd}}. \quad (16)$$

After replacing complex exponentials with trigonometric functions, equation (15) becomes

$$I(q, d) = C \frac{\sin^2\left(\frac{Nqd}{2}\right)}{\sin^2\left(\frac{qd}{2}\right)}, \quad (17)$$

where: C = a constant.

Right-hand side of the equation (17) is approximated to a Gaussian profile:

$$\frac{\sin^2(Nx)}{\sin^2(x)} \approx N^2 e^{-\frac{(Nx)^2}{\pi}}. \quad (18)$$

Using the Gaussian approximation and writing \mathbf{q} as $2\pi/\lambda(\mathbf{u}' - \mathbf{u})$, the intensity equation becomes

$$I(\Delta\mathbf{u}) = Ce^{-\frac{\pi(Nd)^2(\Delta\mathbf{u})^2}{\lambda^2}}. \quad (19)$$

Incident and scattered wave-vector directions are represented by unit vectors \mathbf{u} and \mathbf{u}' respectively in Figure 1 and also shown in Figure 8. The focus point is the \mathbf{u}'' direction which is fixed. In order to find the full contribution to the intensity from this specific angle, we should rotate the crystal in all directions. Instead, it is also possible to keep the crystal fixed and rotate the vector $\mathbf{u}'' - \mathbf{u}$. $(\Delta\mathbf{u})^2$ in equation (19) is equal to $(x - \Delta \sin \theta)^2 + y^2 + (\Delta \cos \theta)^2$. Δ is fixed and integrals should be taken over all values of x and y .

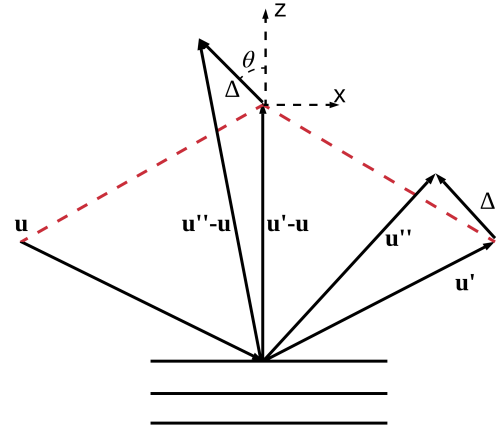


Figure 8: Wave-vectors in the derivation of Scherrer formula.

Equation (19) becomes

$$I(\Delta) = Ce^{-\frac{\pi(Nd)^2\Delta^2 \cos^2 \theta}{\lambda^2}} \int_{-\infty}^{\infty} e^{-\frac{\pi(Nd)^2(x - \Delta \sin \theta)^2}{\lambda^2}} dx \int_{-\infty}^{\infty} e^{-\frac{\pi(Ndy)^2}{\lambda^2}} dy. \quad (20)$$

Results of the integrals above are not Δ dependent functions and they can be added to the constant C:

$$I(\Delta) = C'e^{-\frac{\pi(Nd)^2\Delta^2 \cos^2 \theta}{\lambda^2}}. \quad (21)$$

When $\Delta = 0$, the maximum intensity of the profile is observed,

$$I(\Delta) = I_{max}e^{-\frac{\pi(Nd)^2\Delta^2 \cos^2 \theta}{\lambda^2}}. \quad (22)$$

When $I(\Delta) = I_{max}/2$, the angle represented by Δ is the half of the FWHM of the profile,

$$\frac{1}{2} = e^{-\frac{\pi(Nd)^2w^2}{4\lambda^2 \cos^2 \theta}}. \quad (23)$$

FWHM of the profile becomes

$$w = \frac{2\sqrt{\ln(2)}\lambda}{\sqrt{\pi}Nd \cos \theta}. \quad (24)$$

Equation (24) is the well known Scherrer formula. Number of coherent planes times d-spacing, Nd is the edge dimension of the crystal parallel to $(00l)$ normal. The constant $2\sqrt{\ln(2)}/\sqrt{\pi}$ is dimensionless and equal to 0.94. One can easily see from the derivation that this number not only depends on the shape of the crystallite, but also depends on the plane direction of the material. For instance, a cubic crystallite should have different constants for (001) and (111) planes. However, the exact number of the constant has no significant value since the information of the crystallite shapes are rather uncertain. In this study, it is taken as 0.94.

2.5 Williamson-Hall Model

Crystallite size is not the only reason for broadening in line profiles. Another common reason is the non-uniform (or inhomogeneous) lattice distortion [19]. Main reasons for the non-uniform lattice distortion are defects such as dislocations, anti-phase domain boundaries, faulting and solid solution inhomogeneity.

Lattice parameter of TiAlN highly depends on the Ti and Al content and it is not uniform throughout the material. Thus, microstrain should be taken into account when analyzing the samples. In addition to the Scherrer equation, Williamson-Hall model [20] takes microstrain into account. Assuming that both crystallite size and microstrain contribution have Lorentzian profile, total broadening can be written as the summation of the two (Equation (13)):

$$w_{\text{total}} = \frac{0.94\lambda}{L \cos \theta} + w_{\text{microstrain}}. \quad (25)$$

The contribution of the microstrain can be obtained by differentiating the Bragg's law with respect to 2θ :

$$-\frac{\cos \theta \lambda}{\sin^2 \theta} d\theta = 2d dd_{hkl}. \quad (26)$$

For cubic systems, relationship between lattice parameter and plane spacing is

$$\frac{da}{a} = \frac{dd_{hkl}}{d_{hkl}}. \quad (27)$$

Equation (26) becomes

$$-2 \tan \theta \frac{da}{a} = d2\theta. \quad (28)$$

FWHM of Lorentzian function is two times the scale parameter which is also called as probable error. Multiplying both sides of Equation (28) with 2 yields

$$w_{\text{microstrain}} = 4 \tan \theta \frac{\Delta a}{a}. \quad (29)$$

Final version of the model can be written as

$$w_{total} \cos \theta = 4\varepsilon \sin \theta + \frac{0.94\lambda}{L}, \quad (30)$$

where: ε = Root Mean Square (RMS) of strain.

Equation (30) yields a straight line where ε is the slope and $\frac{0.94\lambda}{L}$ is the intercept. Such a plot is known as a Williamson-Hall plot and is illustrated in Figure 9. The term $\frac{\Delta a}{a}$ is called microstrain in literature frequently and it is the RMS of the strain.

One should not confuse RMS of strain with strain. Strain is non-uniform (or inhomogeneous) and the average of its sum is zero. However its RMS is not zero and it is what Williamson-Hall model provides. A more detailed explanation is made by Guinier [21].

There are two types of imperfections, first and second type. First type of imperfections introduce deviations between the distances of corresponding atoms, but preserve the long range order. An example of this type is thermal agitation. Figure 10 shows example structures with the imperfections of first and second type. In order to see how these imperfections affect the XRD diffractogram, atoms are considered as single electrons and XRD diffractograms are calculated by taking the Fourier transform of the electron densities. First type of imperfections do not contribute to line profile broadening but change the intensity while the second type results in broadening. In both cases, there is a deviation in the lattice parameter. However, standard deviation of d spacing is zero in the first type while it is non zero in the second type. The slope of Williamson-Hall plot is highly influenced by concentration fluctuations of Ti and Al atoms [22] which are second type imperfections. Ideally, if Ti and Al atoms were uniformly dis-

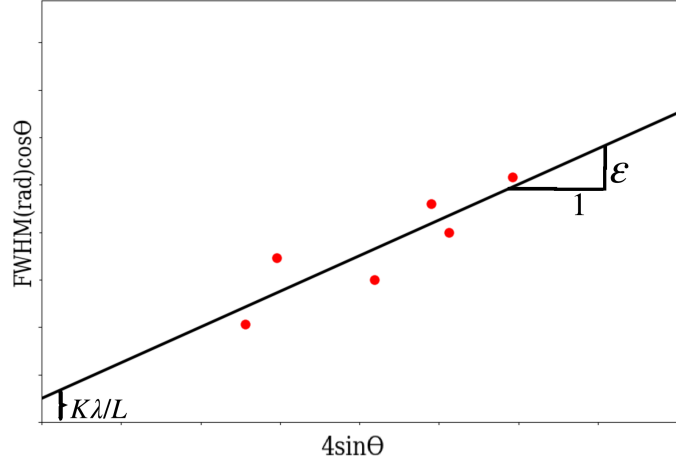
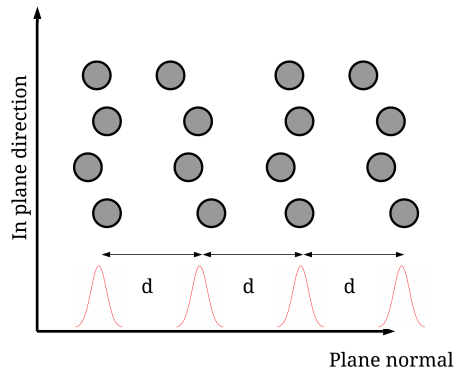
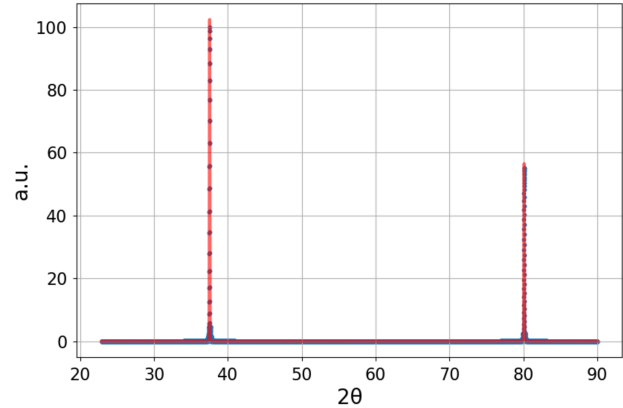


Figure 9: Williamson-Hall plot

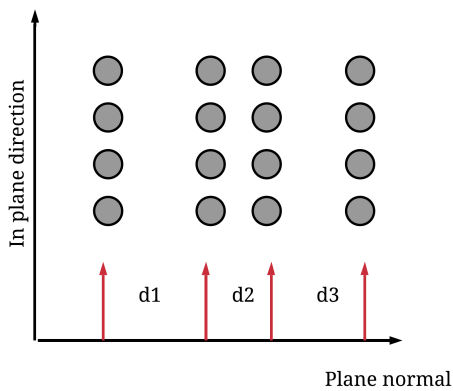
tributed on very large coherent planes, all planes would have the same concentration ratio and d spacing would be the same for all planes as in Figure 10a provided that Vegard's Rule is valid.



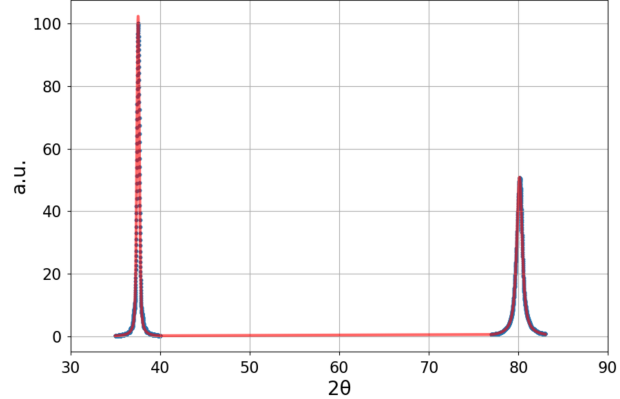
(a) First type of imperfection. Even though the crystal is not perfect, no broadening is observed.



(b) Calculated line profile of first type of imperfection. Thermal agitation does not result in broadening.



(c) Second type of imperfection. Deviations in inter-planar spacing results in broadening.



(d) Calculated line profile of second type of imperfection. Inter-planar spacings are sampled from a Gaussian distribution function.

Figure 10: First and second type of imperfections.

Even though Williamson-Hall model is simple and easy to implement, it has many drawbacks:

- Size and strain contributions are not Lorentzian.
- There are only 6 peaks observed in TiAlN and the uncertainty of the fit is high.
- Taking derivative of Bragg's law does not represent a firm theoretical basis.

2.6 Warren-Averbach Model

Warren-Averbach model [23] involves expressing line profiles in terms of Fourier series. Due to its length, the derivation is not provided in this study. However, a detailed explanation is given by Warren [24]. It is important to mention that Lorentz polarization factor for integrated intensity of diffraction line is different than the factor for a diffraction line profile. Under the assumption of an orthorhombic cell, the profile of $(00l)$ plane can be written as a Fourier series:

$$I(2\theta) = C \sum_{n=1}^{\infty} A_n \cos(2\pi n h_3) + B_n \sin(2\pi n h_3), \quad (31)$$

where: C = a constant,

$$h_3 = \frac{2d \sin \theta}{\lambda}.$$

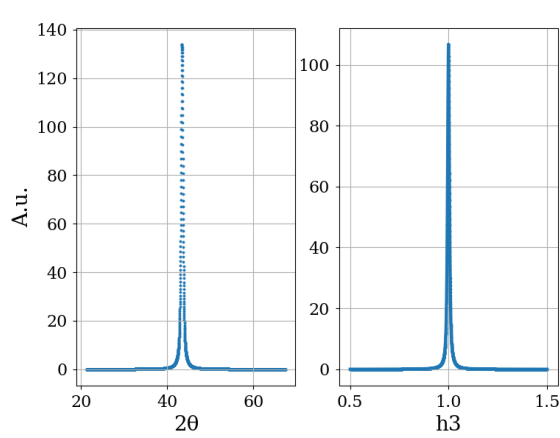
Intensity term on the left hand side of Equation (31) does not take into account the Lorentz polarization factor. For more precise calculations, it should be subtracted before calculating the coefficients. A more detailed discussion is provided by Yinghua [25]. Since pseudo-Voigt profile is symmetric, sine part of the series is zero. By plotting the line profile in the range between $h_3 = l - 1/2$ and $h_3 = l + 1/2$, the set of A_n coefficients is determined. They have arbitrary units so a normalization is done that makes $A_0 = 1$. The cosine coefficients are multiplication of size and strain coefficients:

$$A_n = A_n^{\text{Size}} A_n^{\text{Strain}}. \quad (32)$$

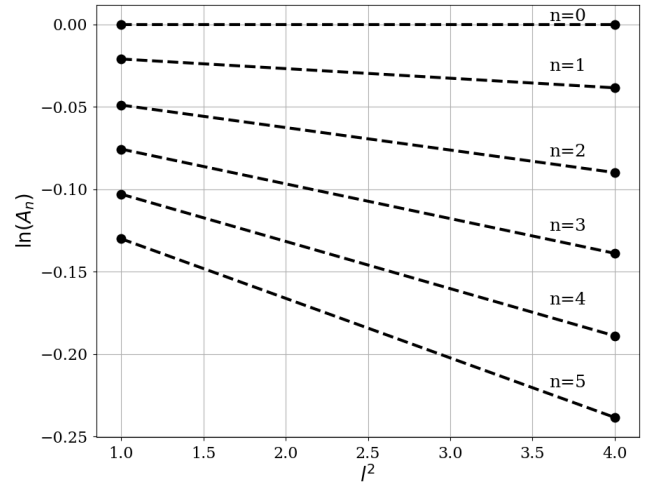
In order to be able to separate size and distortion coefficients, several orders of $(00l)$ plane should be measured. Size coefficient is independent of order l , while distortion depends on it. For small values of l and n , the logarithm of the cosine coefficient can be approximated to

$$\ln A_n(l) = \ln A_n^{\text{Size}} - 2\pi^2 l^2 \langle Z_n^2 \rangle, \quad (33)$$

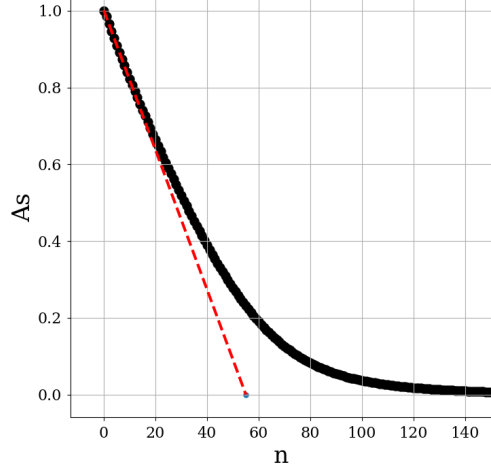
where: Z_n = Displacement of n stacked planes divided by inter-planar spacing.



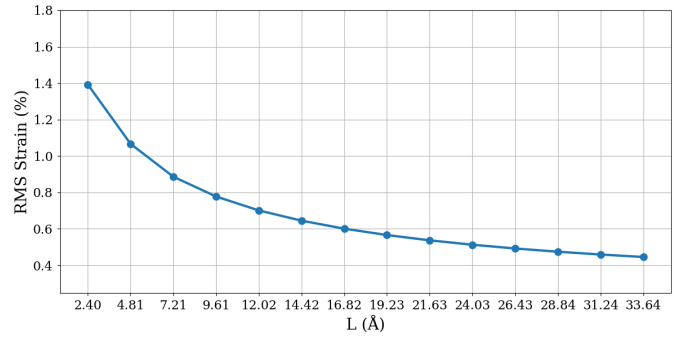
(a) Transform abscissa to h_3 (l) and get the Fourier coefficients of the profile.



(b) Calculate size coefficients and mean square of strain using Equation (33).



(c) First derivative of the size coefficients A_n^{Size} for small n yields average number of stacked planes.



(d) Plot RMS of strain for stack of planes with different size.

Figure 11: Summary of Warren-Averbach analysis.

Figure 11b shows the plot of $\ln A_n(l)$ versus l^2 for (001) and (002) planes. This can be generalized to all crystal systems. Since TiAlN diffraction pattern consists of (111) - (222) and (002) - (004) plane families, it is possible to construct Figure 11b for both [111] and [002] plane normal directions. Intercepts of the lines drawn for each n are the size coefficients and they are plotted in Figure 11c. First derivative (red dashed line) points out the average number of coherent plane stacks. Mean square of the displacement of n neighbouring plane

stack is $\langle \Delta L_n^2 \rangle = d\langle Z_n^2 \rangle$. L_n is equal to d-spacing times number of planes, nd . The ratio $\Delta L_n/L_n$ is the strain and the slope of the line segments in Figure 11b can also be written as $-2\pi^2 n^2 \langle \varepsilon_n^2 \rangle$. Figure 11d shows the calculated RMS values of strain.

2.6.1 Estimation of Crystallite Size Distribution

Contrary to Scherrer formula or Williamson-Hall model, Warren-Averbach model provides the area weighted average in addition to the volume weighted average crystallite size. Before explaining what area and volume weighted average mean, a more important question should be addressed. What does the crystallite size mean? Bertrand [26] introduced that a crystallite is a collection of unit cell columns aligned perpendicularly to the given set of reflecting planes. In other words, the signal measured during XRD experiments is not the result of crystallite size distribution, it is the distribution of unit cell column lengths that governs the size coefficients of line profiles. The j^{th} moment of unit cell column length is defined as

$$\langle L^j \rangle = \frac{\int_0^\infty L^j p(L) dL}{\int_0^\infty p(L) dL}, \quad (34)$$

where: $p(L)$ = unit cell column length distribution.

The area of each column projected onto the reflecting plane is equal. Thus, the area weighted average column length can be written as

$$\langle L \rangle_{\text{area}} = \frac{\int_0^\infty L [p(L) \delta a] dL}{\int_0^\infty [p(L) \delta a] dL} = \langle L^1 \rangle, \quad (35)$$

where: δa = column cross sectional area.

Area weighted average and numerical average are equal since column cross sectional area is

equal for all columns. The volume weighted average of column length distribution is

$$\langle L \rangle_{\text{volume}} = \frac{\int_0^\infty L[p(L)\delta aL]dL}{\int_0^\infty [p(L)\delta aL]dL} = \frac{\langle L^2 \rangle}{\langle L^1 \rangle}, \quad (36)$$

where: δaL = volume of a column with length L.

The relationship between size coefficients and two independent weighted average column lengths is

$$\langle L \rangle_{\text{area}} = \frac{1}{\lim_{L \rightarrow 0} \left(\frac{dA^{\text{Size}}}{dL} \right)}, \quad (37a)$$

$$\langle L \rangle_{\text{volume}} = 2 \int_0^\infty A^{\text{Size}}(L)dL. \quad (37b)$$

Crystallite size distribution function differs significantly from the column length distribution function [27]. Switching between them requires the crystallite shape information of each crystallite. The most commonly reported distribution of crystallite size by far in a powder sample or polycrystalline solid in literature is the log-normal distribution [28]. Normalized log-normal distribution is written as

$$g(D) = \frac{1}{\sqrt{2\pi}D \ln \sigma} \exp \left[-\frac{1}{2} \left(\frac{\ln \frac{D}{D_0}}{\ln \sigma} \right)^2 \right], \quad (38)$$

where: D_0 = Median of distribution,

σ = Variance of distribution.

If $\langle L \rangle_{\text{area}}$ and $\langle L \rangle_{\text{volume}}$ are measured by XRD, under the assumption that crystallites are spherical and diameters have log-normal distribution, it is possible to construct crystallite size distribution. Median and variance of the distribution are related to area and volume weighted averages:

$$\langle L \rangle_{\text{area}} = \frac{2}{3} D_0 \exp \frac{5}{2} \ln^2 \sigma, \quad (39a)$$

$$\langle L \rangle_{\text{volume}} = \frac{3}{4} D_0 \exp \frac{7}{2} \ln^2 \sigma. \quad (39b)$$

If crystallites are assumed to be cubic, following relation is used for orientationally averaged cubic crystallites:

$$\langle L \rangle_{\text{area}} = 0.5373 D_0 \exp \frac{5}{2} \ln^2 \sigma, \quad (40a)$$

$$\langle L \rangle_{\text{volume}} = 0.7227 D_0 \exp \frac{7}{2} \ln^2 \sigma. \quad (40b)$$

Figure 12 shows the log-normal distribution. Equation (33) is an approximation and is valid only for small values of n . Since higher order size coefficients have high uncertainty, $\langle L \rangle_{\text{volume}}$ has low accuracy and calculated distributions do not have critical importance. In addition to XRD measurements, it is also possible to measure crystallite size distribution by direct imaging using transmission electron microscopy (TEM). However, sample preparation and analysis is often challenging [27].

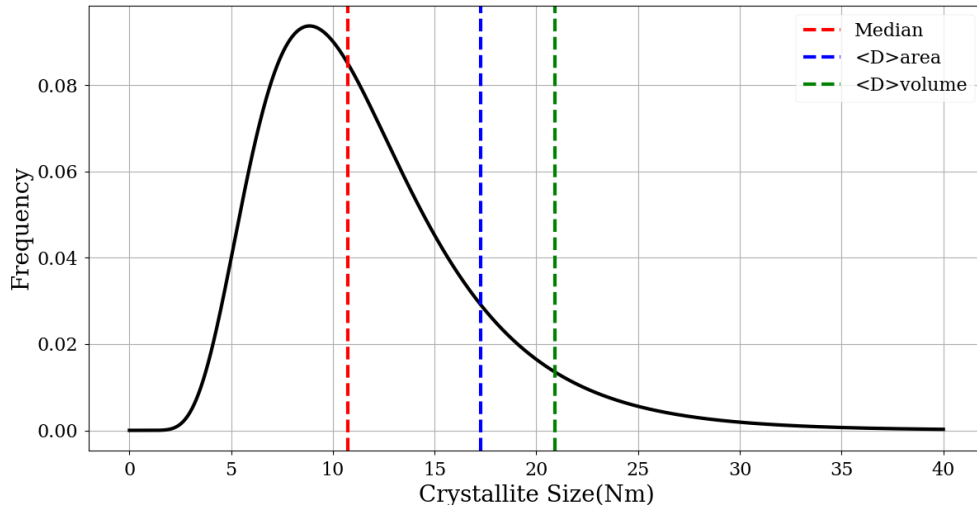


Figure 12: Log-normal distribution of crystallite size.

3 Results and Discussion

3.1 Experimental Details

$\text{Ti}_{0.5}\text{Al}_{0.5}\text{N}$ samples were previously synthesised by high power pulsed magnetron sputtering (HPPMS). The substrate was NaCl sprayed on Al-foil. Thin film flakes were obtained by removing the NaCl in distilled water. Samples were annealed with a heating rate of 40 K/min and the aging time was less than 1 minute. X-Ray diffractograms are measured by both Siemens D5000 diffractometer and Bruker AXS D8 General Area Detection Diffraction System (GADDS). In both cases the voltage and current of the Cu X-ray source are set to 40 kV and 40 mA, respectively. D5000 measurements are done in $\theta\text{-}\theta$ Bragg-Brentano geometry. 2θ ranges of 35° to 100° are scanned at a step size of 0.02° and the measurement time is 25 seconds per step. GADDS measurements are also done in $\theta\text{-}\theta$ Bragg-Brentano geometry. However radiation source, sample and detector are fixed in space since an area detector is used. Every peak profile is measured individually and the measurement time was 1 hour for each profile. In Section 2.3 it is discussed that instrumental broadening is larger in GADDS compared to D5000. Nevertheless, GADDS results are used in this study.

The reason is that background intensities make Warren-Averbach analysis impossible to implement for D5000 results. Appendix A shows diffractograms of the same sample measured with D5000 and GADDS. While there is no need for a background function to fit the profile in GADDS, a 6th degree polynomial is used in D5000 measurement. The reason for this bump is the glass substrate and the binder which holds the powder. Tails of the profiles have significant importance in Warren-Averbach analysis and since the exact form of background function is

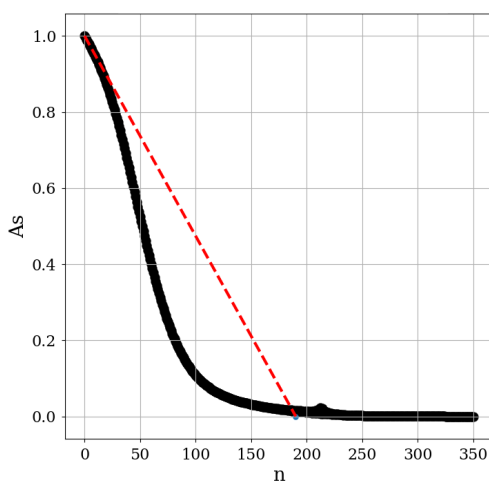


Figure 13: Hook effect observed in D5000 measurements.

not known, it is not possible to get reliable results.

It is frequently reported in literature that, sometimes experimentally determined size coefficients (Figure 11c) have a concave hook at small values of n . This is known as "hook effect" and is shown in Figure 13. According to Warren [29], this phenomena is principally impossible and it is an indication that something is wrong in the measurements. It is observed in D5000 measurements and strongly depends on background intensity function. In other words, if another function is used instead of 6th degree polynomial, line profiles change and so do the size coefficients. Nonetheless, there is no consensus on hook effect. Wilkens [30] theoretically calculates that small angle grain boundaries result in hook effect. Measured X-Ray diffractograms of samples annealed at different temperatures are given in Figure 14. Even though there is no significant difference between them, in the following chapters it is shown that they contain important amount of information.

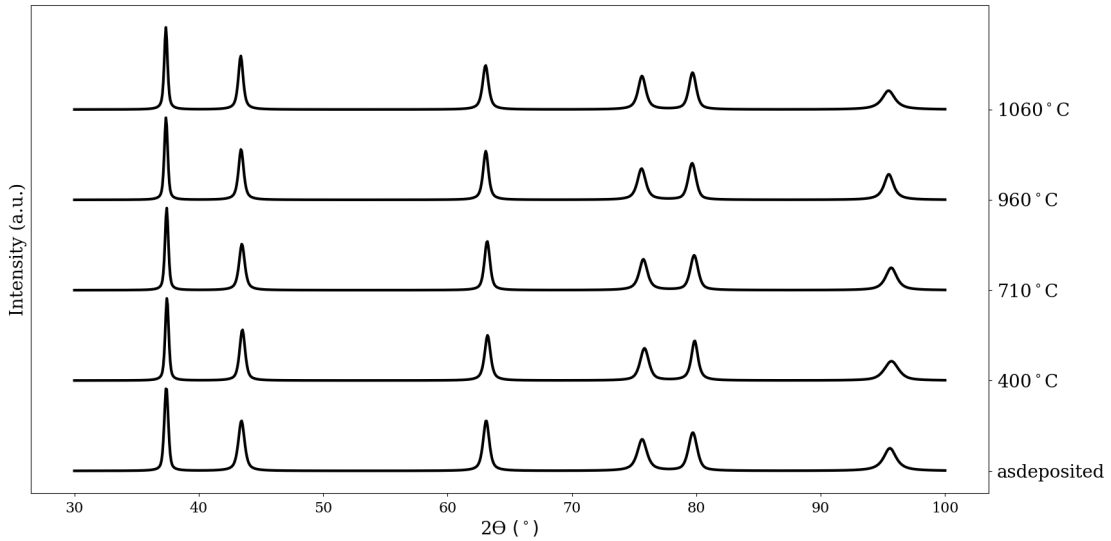


Figure 14: Measured diffractograms at different annealing samples.

3.2 Crystallite Size Comparison

It is reasonable to use Scherrer formula for strain free materials. However, even though it is assumed that material is defect free, TiAlN samples will show high amount of inhomogeneous strain due to the chemical fluctuations of Ti and Al atoms. Inapplicability of Scherrer equation can be observed in a Williamson-Hall (W-H) plot. Figure 15 shows the W-H plot

of as deposited sample. If microstrain contribution in Equation (30) is assumed to be zero, FWHM of the profiles will be only size dependent and the slope of the fit will be zero. This case is shown as green dashed line. It does not fit to the measurement. The results

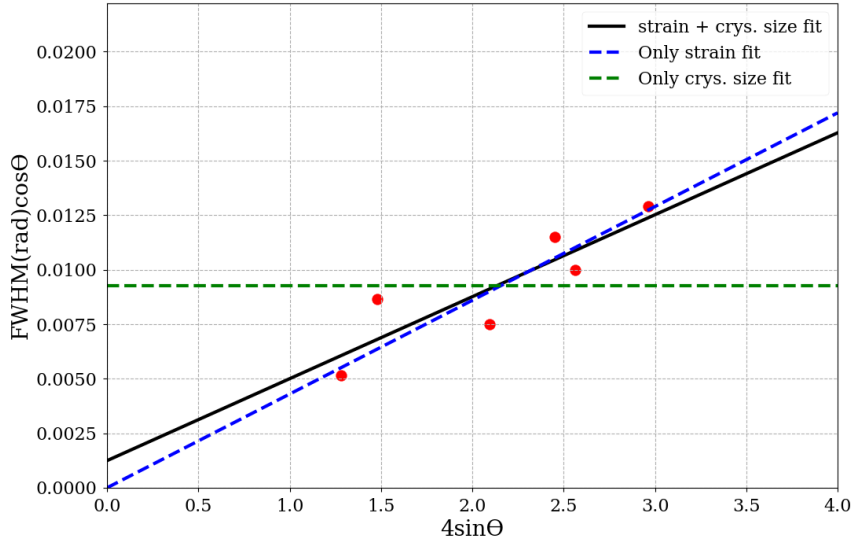
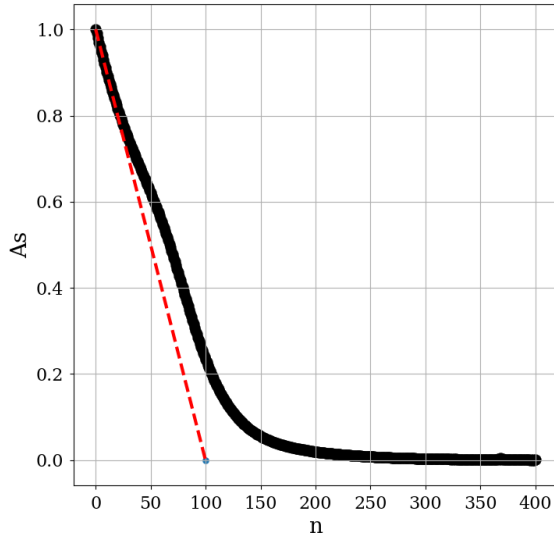


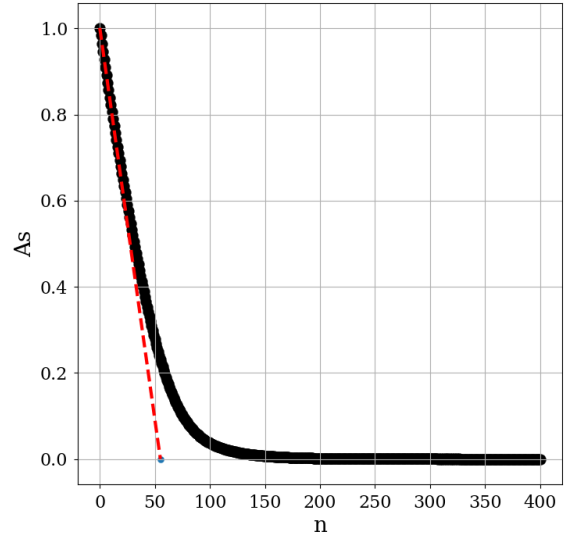
Figure 15: Williamson - Hall plot of as deposited TiAlN sample.

provided in Table 2 are calculated from individual line profiles of (200) and (111) planes and are volume weighted averages. Intercept of the fitted line in W-H model provides the crystallite size and it estimates that average crystallites are larger than 100 nanometers for all samples. Scherrer equation is only valid for small average crystallite sizes and so does W-H model. While Scherrer equation can not get the microstrain, W-H model does not yield realistic crystallite size. Compared to these two models, Warren-Averbach (W-A) analysis has the strongest theoretical basis and should be used for more reliable average crystallite size calculations. Figure 16 shows the size coefficients of (200) and (111) profiles of as deposited sample. The numbers provided in W-A columns of Table 2 are area weighted (or arithmetic) averages of coherent column lengths. It is also possible to obtain volume weighted averages. Since uncertainty of higher index size coefficients is high, results are not provided in Table 2. W-A and W-H plots that are used in order to obtain results shown in Table 2 are provided in Appendix B.

Scherrer equation does not take into account structural defects and chemical fluctuations, so



(a) Coefficients of (111)-(222) planes. Average number of coherent planes is 100.



(b) Coefficients of (002)-(004) planes. Average number of coherent planes is 55.

Figure 16: Size coefficients of as deposited sample.

it yields a lower boundary value. However, W-A analysis results are smaller than the Scherrer formula results. This is due to the weight of the averages. Volume weighted average is larger than the arithmetic average. Thus, it is expected to observe smaller values in W-A analysis. Average number of coherent unit cell columns in [111] is larger than the [200]. It shows that crystallites have columnar shape rather than equiaxed shape. It is also an indication that the [111] direction is favoured during crystal growth. Another important point to mention is, sample annealed at 1060 °C has similar averages in (200) and (111) profiles. This result supports the equiaxed grain formation around 1100 °C reported in literature [31].

Table 2: Calculated average crystallite sizes

Anneal Temp.	Scherrer(200)	Scherrer(111)	W-H	W-A(200)	W-A(111)
As deposited	16.7 nm	28.1 nm	116.3 nm	11.4 nm	24.0 nm
400°C	19.2 nm	37.1 nm	>200 nm	15.6 nm	24.1 nm
710°C	18.7 nm	27.2 nm	>200 nm	11.0 nm	23.3 nm
960°C	18.9 nm	26.5 nm	>200 nm	10.5 nm	21.5 nm
1060°C	23.2 nm	43.7 nm	>200 nm	24.6 nm	21.6 nm

3.3 Microstrain Comparison

Figure 17 summarizes the calculated RMS values of strain according to W-H and W-A models. W-H model provides a single value which is the average microstrain and it is shown as red dashed line. As the distance L increases, RMS of microstrain decreases in all samples. Physical explanation is as follows.

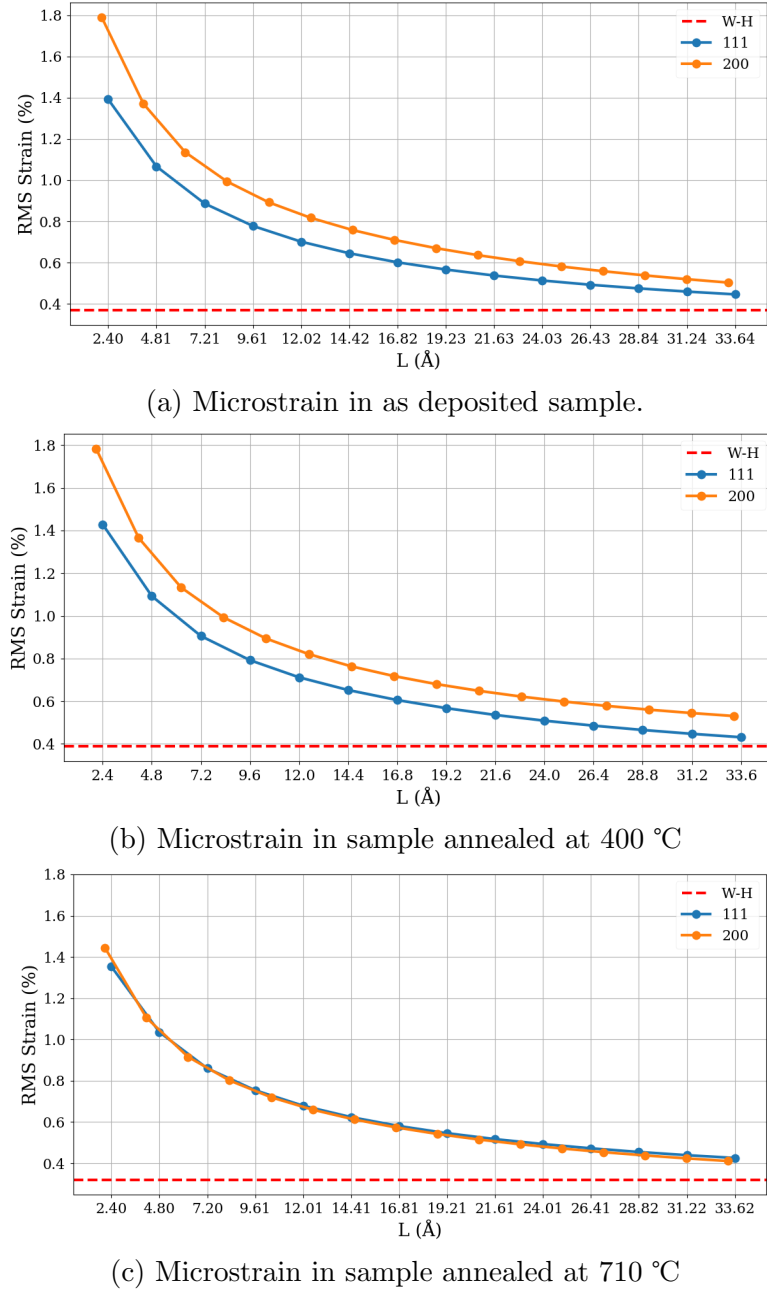
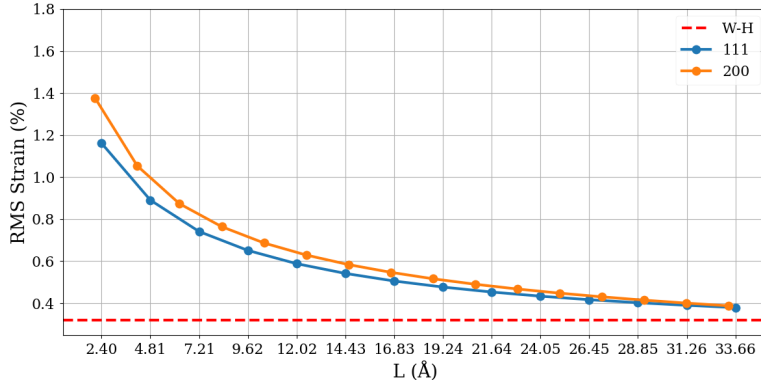
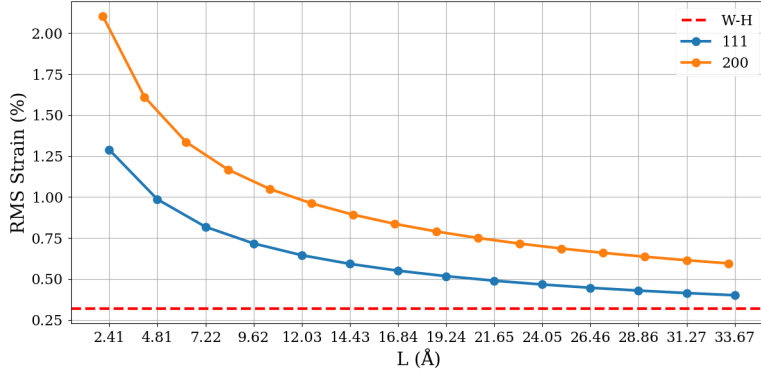


Figure 17: Microstrain at different annealing temperatures.



(d) Microstrain in sample annealed at 960 °C



(e) Microstrain in sample annealed at 1060 °C

Figure 17: RMS of strain at different annealing temperatures. (cont.)

Figure 18 shows two super-cells which can be used to represent the coherent planes. The standard deviation of distortion divided by distance ($\frac{\Delta L}{L}$) is larger in L_1 compared to L_2 . Microstrain is not isotropic within the samples. One reason might be the non-uniform distribution of metal ions. Differences in chemical fluctuations within the (111) and (200) planes

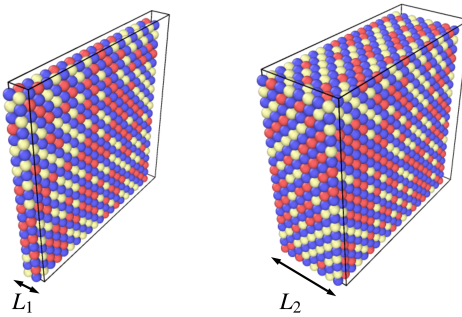
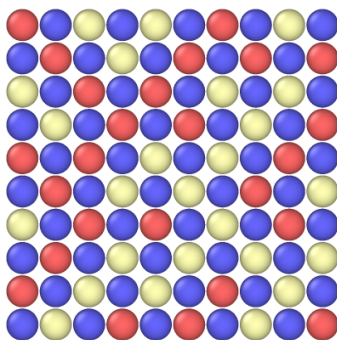


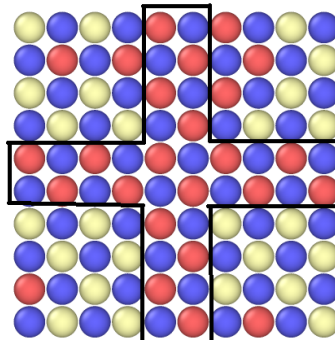
Figure 18: Physical meaning of calculated strains.

might lead to anisotropic deviations in microstrain. The second reason is the existence of defects. Defects create strain fields around them and this field depends on the spatial position of the defects (e.g. slip planes) combined with the elasticity tensor of the material. Figure 17c is a very strong indication that the latter one is the case. Growth defects are generated due to the rapid quenching and energetic particle bombardment [32] and temperatures around 700 °C were reported for the annihilation of growth defects [33, 31]. As the defects vanish from the elastically anisotropic TiAlN [34], Figure 17a evolves to Figure 17c. Calculation of *dislocation contrast factors* [35] enables quantifying the dislocation broadening of the line profiles. The elastic properties of the material, displacement field of the dislocations and geometric orientation of the diffraction vector relative to the dislocation slip-system are incorporated into the analysis and the method is known as modified Warren-Averbach method [35]. Modified W-A model makes dislocation density analysis possible for cold worked samples. It is not discussed in this study.

As the annealing temperature increases from 710 °C to 1060 °C, the microstrain gap between [100] and [111] directions starts to widen. This observation can be attributed to beginning of spinodal decomposition. Microstrain in [100] direction is significantly increased. It indicates that c-AlN clusters are forming on (200) planes. Findings in this study support surface directed spinodal decomposition [31, 36, 37, 38]. In order to explain how c-AlN clusters that are elongated in [100] direction affect the microstrain, a 2D structure example is given. In Figure 19a metal atoms are uniformly distributed and in Figure 19b c-AlN is clustered



(a) Uniformly distributed metal atoms.



(b) Al atoms cluster on $\{10\}$ planes.

Figure 19: 2D explanation of increased strain gap at higher annealing temperatures.

on (01) and (10) planes. N, Al and Ti atoms are represented by blue, red and yellow respectively. If chemical compositions of each {01} and {11} planes are counted, one can see that standard deviation of Al content (%) on {01} planes is equal to 13.4 in Figure 19a, while it is 30.0 in Figure 19b. However, if Al content is counted on {11} planes, there is no significant change in standard deviation. It is equal to 11.2 in Figure 19a, while it is 10.2 Figure 19b.

3.4 Conclusion & Future Work

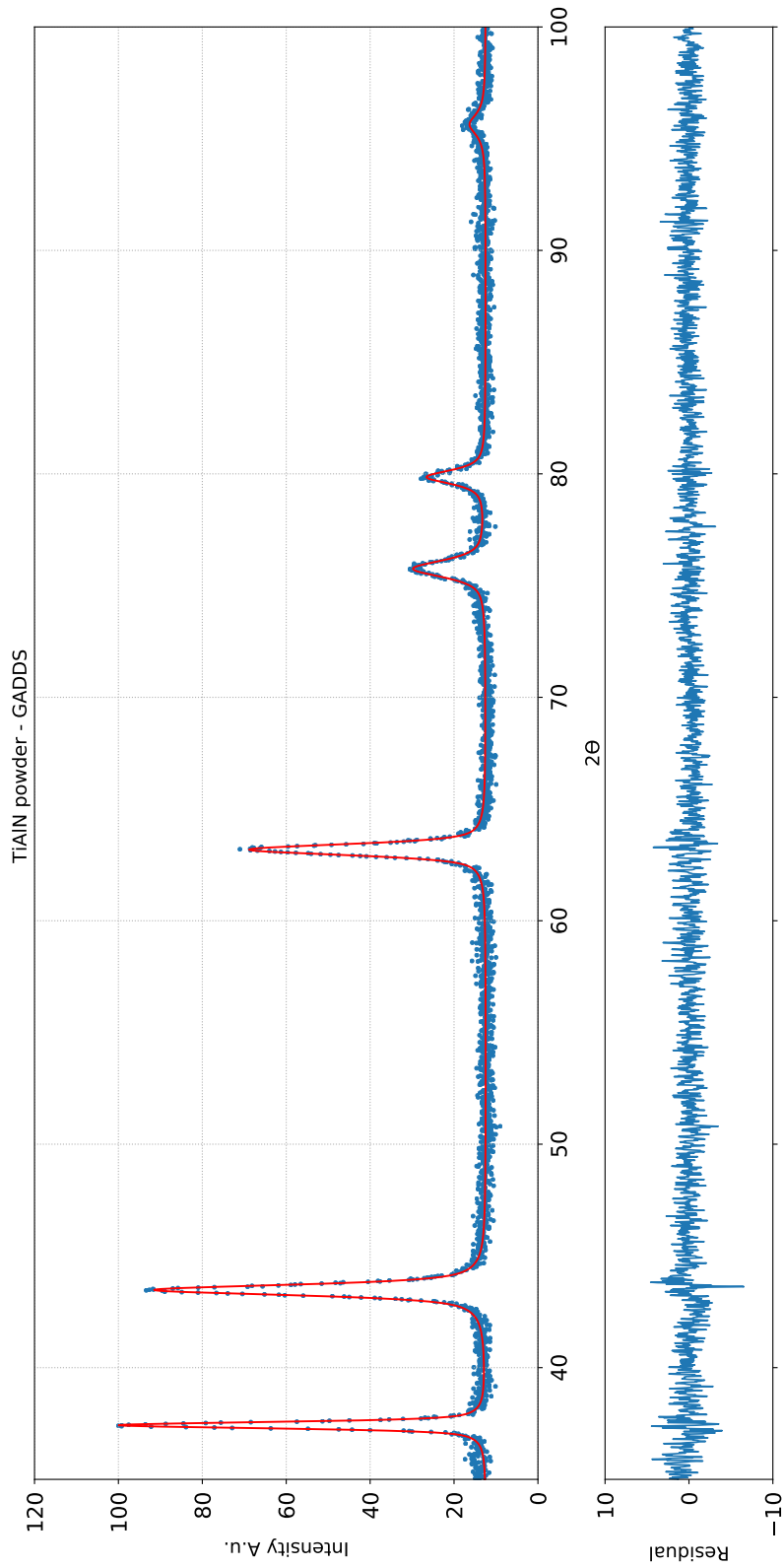
Bragg's law is useful for determination of average lattice parameters, but it does not yield any information about non-perfect crystals. Line profile analysis is required for this purpose. Scherrer equation can not be applied to materials with high microstrain such as TiAlN. Williamson-Hall model is simple to implement and takes into account the microstrain, but it does not rely on a firm theoretical basis and yields unrealistic average crystallite size. Warren-Averbach analysis is an advanced Fourier analysis of line profiles and is able to cover size and microstrain information if at least 2 set of line profiles of a plane appears. Since both (111)-(222) and (200)-(400) planes are present in TiAlN diffractograms, it also provides directional information. In this study, it is shown that cheap and cost effective laboratory XRD equipment is capable of giving an insight into phenomenal material characteristics such as:

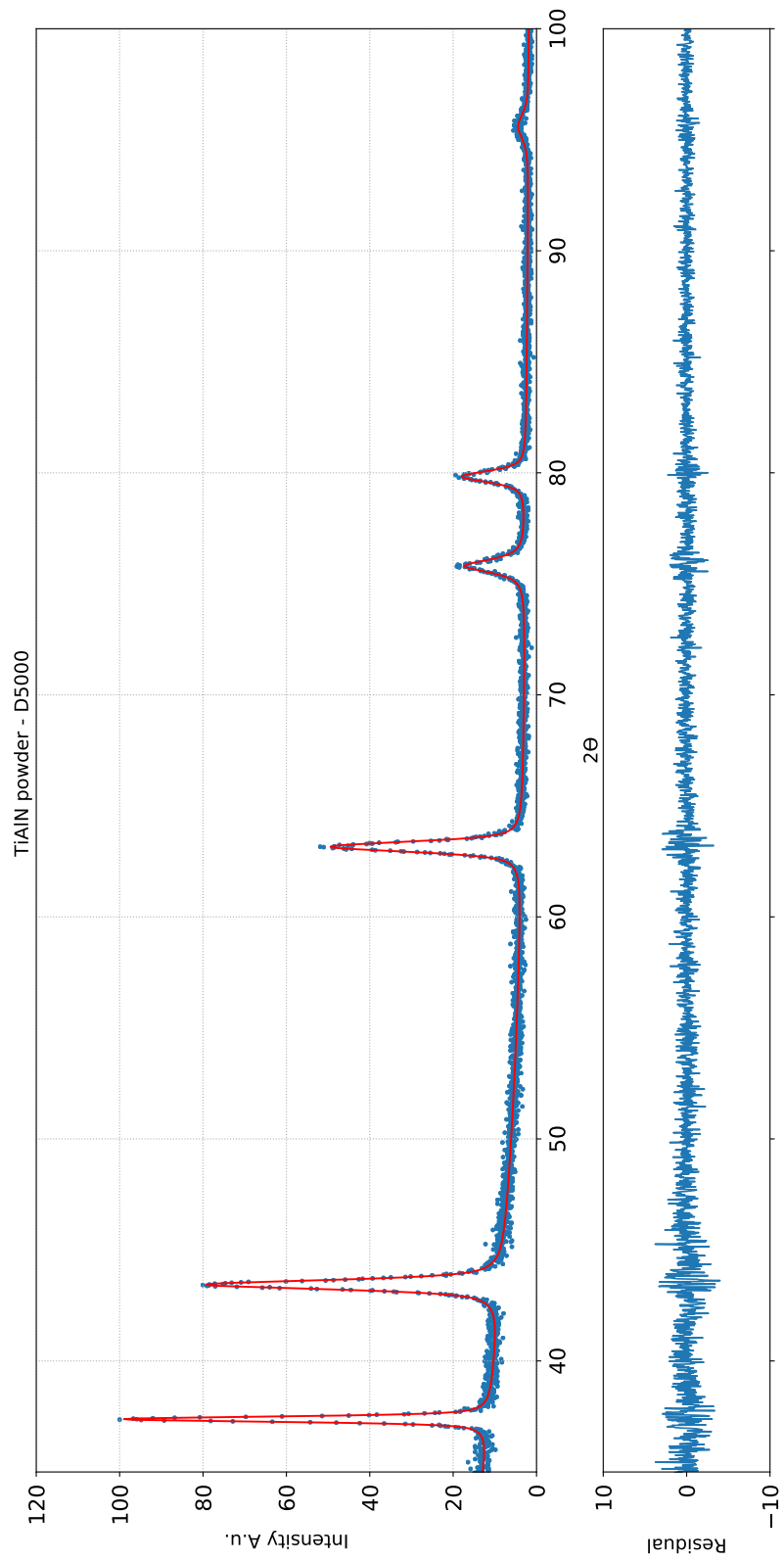
- Crystallite shape and distribution,
- Preferential growth direction,
- Annihilation of growth defects,
- Surface-directed spinodal decomposition.

There is no information provided in this mini-thesis about the accuracy and reliability of the Warren-Averbach model. As a future work, the model can be applied to different sets

of materials with better measurements (e.g. synchrotron) and the results can be verified via direct imaging transmission electron microscopy (TEM) results.

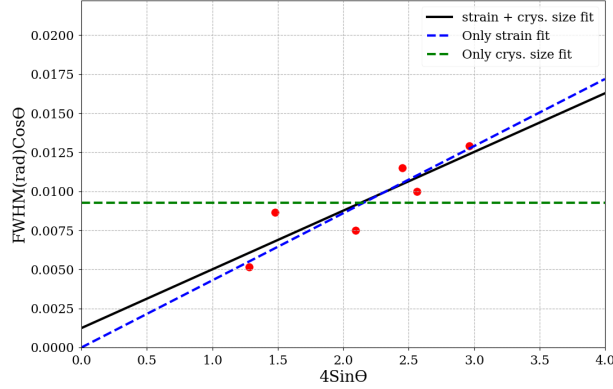
A Appendix



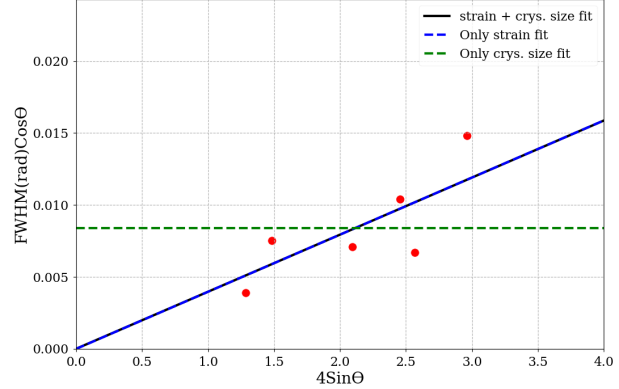


B Appendix

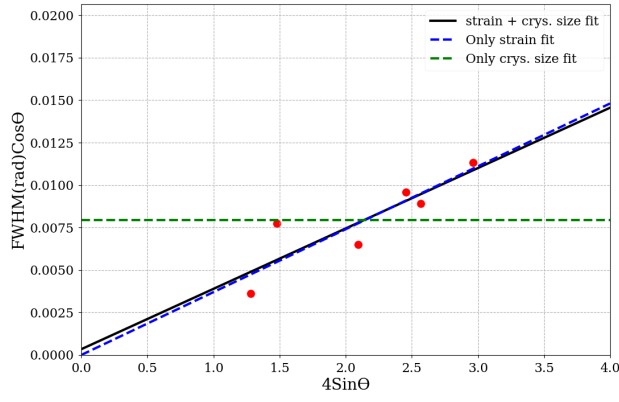
as deposited



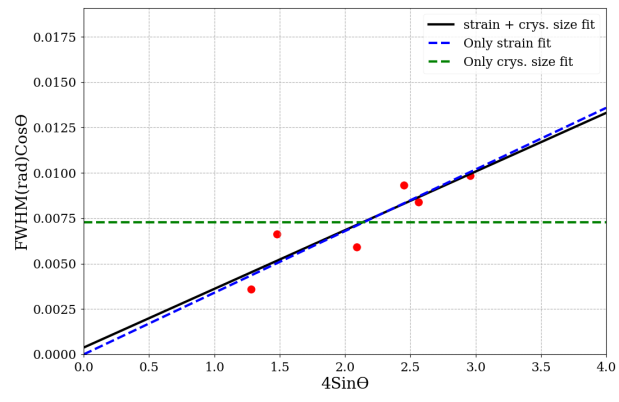
400°C



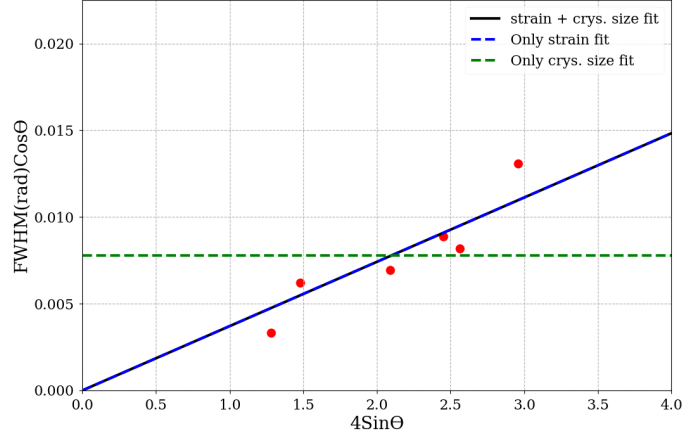
710°C



960°C

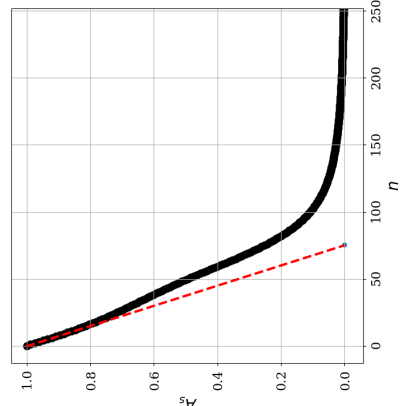


1060°C



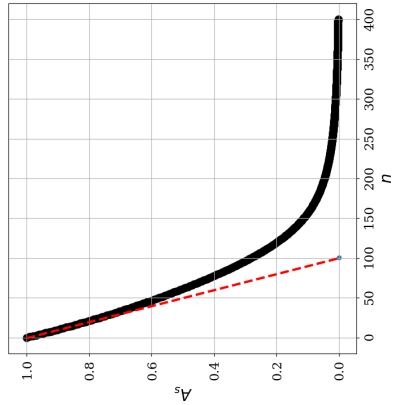
as deposited

400°C
(200)

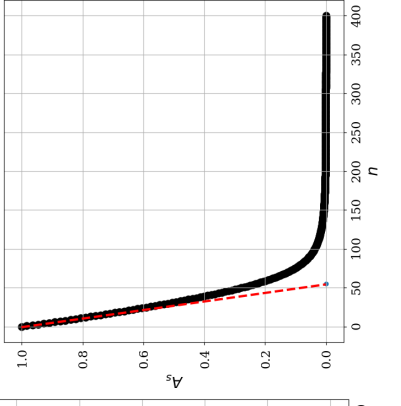


(111)

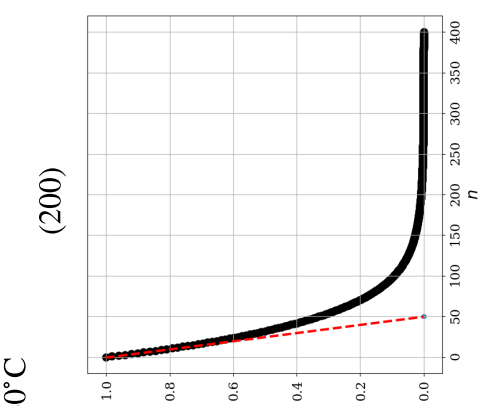
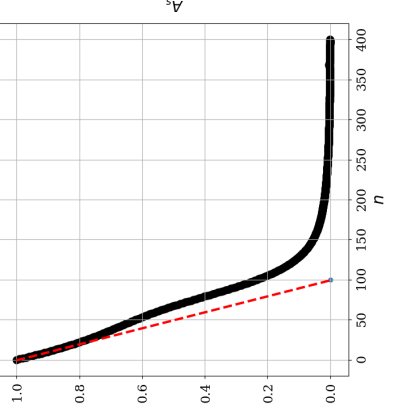
400°C



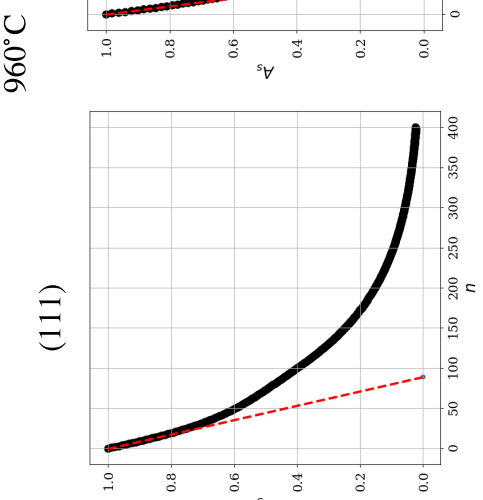
(200)



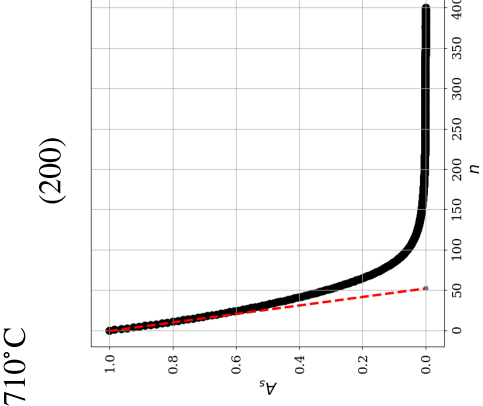
(111)



960°C
(200)

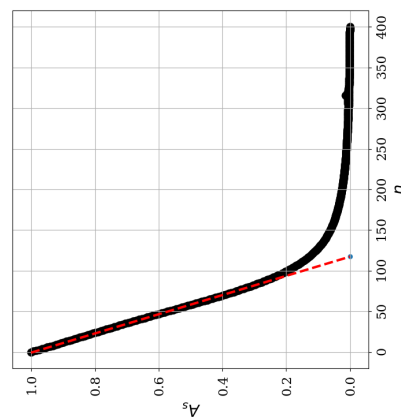
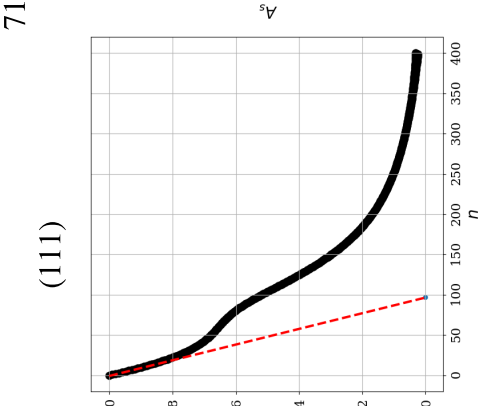


710°C
(200)
1060°C

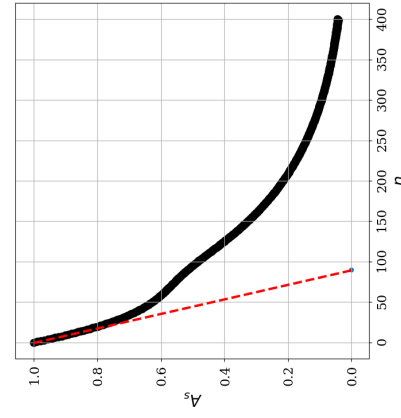


(111)

710°C
(200)



(111)



References

- [1] J. J. de Pablo, B. Jones, C. L. Kovacs, V. Ozolins, and A. P. Ramirez, “The Materials Genome Initiative, the interplay of experiment, theory and computation,” *Current Opinion in Solid State and Materials Science*, vol. 18, pp. 99–117, Apr. 2014.
- [2] B. D. Cullity, *Elements of X-ray diffraction*. Addison-Wesley series in metallurgy and materials, Reading, Mass: Addison-Wesley Pub. Co, 2d ed ed., 1978. p. 108.
- [3] R. W. Harrison, “Phase problem in crystallography,” *J. Opt. Soc. Am. A*, vol. 10, p. 1046, May 1993.
- [4] D. Balzar, “X-ray diffraction line broadening: modeling and applications to high-Tc superconductors,” *J. RES. NATL. INST. STAN.*, vol. 98, p. 321, May 1993.
- [5] E. Prince, H. Fuess, T. Hahn, H. Wondratschek, U. Müller, U. Shmueli, E. Prince, A. Authier, V. Kopsk, D. B. Litvin, M. G. Rossmann, E. Arnold, S. Hall, and B. McMahon, eds., *International Tables for Crystallography: Mathematical, physical and chemical tables*, vol. C of *International Tables for Crystallography*. Chester, England: International Union of Crystallography, 1 ed., Oct. 2006. p. 578 - 580.
- [6] C. Kittel, *Introduction to solid state physics*. Hoboken, NJ: Wiley, 8th ed ed., 2005. p. 42.
- [7] P. Hohenberg and W. Kohn, “Inhomogeneous Electron Gas,” *Phys. Rev.*, vol. 136, pp. B864–B871, Nov. 1964.
- [8] A. Zunger, S.-H. Wei, L. G. Ferreira, and J. E. Bernard, “Special quasirandom structures,” *Phys. Rev. Lett.*, vol. 65, pp. 353–356, July 1990.
- [9] J. P. Perdew, K. Burke, and M. Ernzerhof, “Generalized Gradient Approximation Made Simple,” *Phys. Rev. Lett.*, vol. 77, pp. 3865–3868, Oct. 1996.

- [10] T. Egami and S. J. L. Billinge, *Underneath the Bragg peaks: structural analysis of complex materials*. No. volume 16 in Pergamon materials series, Amsterdam: Elsevier, second edition ed., 2012. p. 29.
- [11] M. De Graef and M. E. McHenry, *Structure of materials: an introduction to crystallography, diffraction and symmetry*. Cambridge: Cambridge University Press, 2007. p. 318.
- [12] M. Newville, T. Stensitzki, D. B. Allen, and A. Ingargiola, “LMFIT: Non-Linear Least-Square Minimization and Curve-Fitting for Python,” Sept. 2014.
- [13] M. Birkholz, P. F. Fewster, and C. Genzel, *Thin film analysis by X-ray scattering*. Weinheim: Wiley-VCH, 2006. p. 97.
- [14] D. R. Black, D. Windover, A. Henins, J. Filliben, and J. P. Cline, “Certification of Standard Reference Material 660B,” *Powder Diffr.*, vol. 26, pp. 155–158, June 2011.
- [15] D. R. Black, D. Windover, M. H. Mendenhall, A. Henins, J. Filliben, and J. P. Cline, “Certification of Standard Reference Material 1976B,” *Powder Diffr.*, vol. 30, pp. 199–204, Sept. 2015.
- [16] G. Caglioti, A. Paoletti, and F. Ricci, “Choice of collimators for a crystal spectrometer for neutron diffraction,” *Nuclear Instruments*, vol. 3, pp. 223–228, Oct. 1958.
- [17] J. I. Langford and D. Lour, “Powder diffraction,” *Rep. Prog. Phys.*, vol. 59, pp. 131–234, Feb. 1996.
- [18] P. Scherrer, “Bestimmung der inneren Struktur und der Größe von Kolloidteilchen mittels Röntgenstrahlen,” in *Kolloidchemie Ein Lehrbuch*, pp. 387–409, Berlin, Heidelberg: Springer Berlin Heidelberg, 1912.
- [19] A. R. Stokes and A. J. C. Wilson, “The diffraction of X-rays by distorted crystal aggregates - I,” *Proc. Phys. Soc.*, vol. 56, pp. 174–181, May 1944.

- [20] G. Williamson and W. Hall, “X-ray line broadening from filed aluminium and wolfram,” *Acta Metallurgica*, vol. 1, pp. 22–31, Jan. 1953.
- [21] A. Guinier, *X-ray diffraction in crystals, imperfect crystals, and amorphous bodies*. San Francisco: W.H. Freeman, 1963. Ch. 6.
- [22] C. Wüstefeld, D. Rafaja, M. Dopita, M. Motylenko, C. Baehtz, C. Michotte, and M. Kathrein, “Decomposition kinetics in Ti_{1-x}Al_xN coatings as studied by in-situ X-ray diffraction during annealing,” *Surface and Coatings Technology*, vol. 206, pp. 1727–1734, Dec. 2011.
- [23] B. E. Warren and B. L. Averbach, “The Effect of Cold Work Distortion on X Ray Patterns,” *Journal of Applied Physics*, vol. 21, pp. 595–599, June 1950.
- [24] B. E. Warren, *X-ray diffraction*. New York: Dover Publications, dover ed ed., 1990. Ch. 13.
- [25] W. Yinghua, “Lorentz polarization factor for correction of diffraction-line profiles,” *J Appl Crystallogr*, vol. 20, pp. 258–259, June 1987.
- [26] E. F. Bertaut, “Raies de DebyeScherrer et repartition des dimensions des domaines de Bragg dans les poudres polycristallines,” *Acta Cryst*, vol. 3, pp. 14–18, Jan. 1950.
- [27] C. E. Kril and R. Birringer, “Estimating grain-size distributions in nanocrystalline materials from X-ray diffraction profile analysis,” *Philosophical Magazine A*, vol. 77, pp. 621–640, Mar. 1998.
- [28] J. I. Langford, D. Lour, and P. Scardi, “Effect of a crystallite size distribution on X-ray diffraction line profiles and whole-powder-pattern fitting,” *J Appl Crystallogr*, vol. 33, pp. 964–974, June 2000.
- [29] B. E. Warren, *X-ray diffraction*. New York: Dover Publications, dover ed ed., 1990. p. 272.

- [30] M. Wilkens, “Diffraction line broadening of crystals containing small-angle boundaries,” *J Appl Crystallogr*, vol. 12, pp. 119–125, Feb. 1979.
- [31] A. Hörling, L. Hultman, M. Odén, J. Sjölén, and L. Karlsson, “Thermal stability of arc evaporated high aluminum-content TiAlN thin films,” *Journal of Vacuum Science & Technology A: Vacuum, Surfaces, and Films*, vol. 20, pp. 1815–1823, Sept. 2002.
- [32] M. to Baben, M. Hans, D. Primetzhofer, S. Evertz, H. Ruess, and J. M. Schneider, “Unprecedented thermal stability of inherently metastable titanium aluminum nitride by point defect engineering,” *Materials Research Letters*, pp. 1–12, Sept. 2016.
- [33] P. H. Mayrhofer, A. Hörling, L. Karlsson, J. Sjölén, T. Larsson, C. Mitterer, and L. Hultman, “Self-organized nanostructures in the TiAlN system,” *Appl. Phys. Lett.*, vol. 83, pp. 2049–2051, Sept. 2003.
- [34] F. Tasndi, I. A. Abrikosov, L. Rogström, J. Almer, M. P. Johansson, and M. Odén, “Significant elastic anisotropy in Ti_{1x}Al_xN alloys,” *Appl. Phys. Lett.*, vol. 97, p. 231902, Dec. 2010.
- [35] T. Ungar, I. Dragomir, A. Revesz, and A. Borbely, “The contrast factors of dislocations in cubic crystals: the dislocation model of strain anisotropy in practice,” *J Appl Crystallogr*, vol. 32, pp. 992–1002, Oct. 1999.
- [36] F. Adibi, I. Petrov, L. Hultman, U. Wahlström, T. Shimizu, D. McIntyre, J. E. Greene, and J. Sundgren, “Defect structure and phase transitions in epitaxial metastable cubic Ti_{0.5}Al_{0.5}N alloys grown on MgO(001) by ultrahighvacuum magnetron sputter deposition,” *Journal of Applied Physics*, vol. 69, pp. 6437–6450, May 1991.
- [37] A. Knutsson, I. C. Schramm, K. Asp Grönhagen, F. Mücklich, and M. Odén, “Surface directed spinodal decomposition at TiAlN/TiN interfaces,” *Journal of Applied Physics*, vol. 113, p. 114305, Mar. 2013.

- [38] L. Rogström, J. Ullbrand, J. Almer, L. Hultman, B. Jansson, and M. Odén, “Strain evolution during spinodal decomposition of TiAlN thin films,” *Thin Solid Films*, vol. 520, pp. 5542–5549, June 2012.